Title

New Constitutive Model for Interface Elements in Finite-Element Modeling of Masonry

Journal

Journal of Engineering Mechanics, 145(5)

ISSN

0733-9399

Authors

Kumar, N

Barbato, M

Publication Date

2019-05-01

DOI

10.1061/(ASCE)EM.1943-7889.0001592

Peer reviewed

New Constitutive Model for Interface Elements in Finite-Element Modeling of Masonry

Nitin Kumar[1], S.M.ASCE; and Michele Barbato[2], M.ASCE

ABSTRACT

A new interface element's constitutive model is proposed in this study for analyzing masonry using simplified micro-modeling (SMM) approach, in which mortar and two unit-mortar interfaces are lumped into a zero-thickness joint (modeled using an interface element) between expanded masonry units. The new model is capable of simulating tension cracking, shear slipping, and compression failure and is defined by a convex composite failure surface consisting of a tension-shear and a compression cap failure criterion. It removes the singularity in the tension-shear region but not in the compression-shear region. In addition, the proposed model is based on the hypothesis of strain hardening. The robustness and computational cost of the proposed model are compared to different constitutive models (which are based on three, two and single failure criterion) that have been widely used in the literature to describe masonry behavior through a series of one-element tests and through the comparison of finite element (FE) response simulation of an unreinforced masonry shear wall. The FE response results indicates that the proposed constitutive model is more efficient than and at least as accurate as the other constitutive models for analyzing masonry using SMM approach.

Keywords: Finite element method; Simplified micro-modeling; Interface element; Constitutive model; Masonry walls.

Introduction

[1] Ph.D. scholar, Department of Civil & Environmental Engineering, University of California Davis, One Shields Avenue, Ghausi Hall**,** Davis, California 95616; Email: ntnkumar@ucdavis.edu

[2] Professor, Department of Civil & Environmental Engineering, University of California Davis, One Shields Avenue, 3149 Ghausi Hall**,** Davis, California 95616; Email: mbarbato@ucdavis.edu

Finite element (FE) modeling of masonry structures is a very complex problem in computational mechanics, which continues to attract the interest of the research community after several decades of investigations. Several FE approaches have been proposed, with different levels of accuracy, computational cost, and information details (Lourenço 1996; Pelà 2009). The highest level of accuracy and detail on the mechanical behavior of masonry could be achieved using the FE micro-modeling approach, in which different masonry components, i.e., masonry units (bricks/blocks) and mortar, are distinctly represented through continuum elements, and the unit-mortar interface is represented by interface elements (Lourenço 1996). Thus, micro-modeling explicitly addresses the intrinsic discontinuity and heterogeneity of masonry elements. However, it is also computationally very intensive and, thus, rarely employed for analysing masonry. The computational cost can be reduced by lumping mortar and two unit-mortar interfaces into a zero-thickness joint (generally modeled using an interface element) between expanded masonry units (Page 1978; Lourenço 1996). This modelling approach is referred to as simplified micro-modeling (SMM) and has been widely employed to investigate the local behavior of masonry (Page 1978; Lourenço 1996; Giambanco et al. 2001; Spada et al. 2009; Dolatshahi and Aref 2011; Macorini and Izzuddin 2011; Aref and Dolatshahi 2013; Kumar et al. 2014a).

The capability of the SMM approach to simulate the mechanical response of masonry properly relies upon the accuracy and robustness of the employed interface element, which relates the traction vector with the relative displacement vector. In fact, in most SMM approaches, the nonlinearity of the system is often concentrated in the interface element, and masonry units are assumed to be elastic in nature (Page 1978; Lotfi and Shing 1994; Lourenço 1996; Chaimoon and Attard 2007; Dolatshahi and Aref 2011; Macorini and Izzuddin 2011). Hence, interface elements should be able to describe all major failure mechanisms of masonry under multi-axial stress

conditions (Page 1983; Dhanasekar et al. 1985; Andreaus 1996; Lourenço 1996; Cuellar-Azcarate 2016), which include: (a) cracking of masonry units in direct tension, (b) cracking of mortar joints, (c) bed or head joint failure due to sliding under normal stress, (d) diagonal tension cracking of masonry units, and (e) masonry crushing.

Zero-thickness interface elements formulated in terms of traction-separation relationships were originally introduced by Goodman et al. (1968) to model discontinuity in rock mechanics. Page (1978) introduced the use of interface elements between elastic continuum elements (representing expanded masonry units) in failure analysis of masonry. The non-linear behavior of masonry was simulated through the interface behavior, which was modeled through a constitutive model that included a brittle failure in tension and hardening in shear/compression. However, compression (crushing) failure was not included in the interface elements (e.g., Page 1978; Lotfi and Shing 1994; Anand and Yalamanchili 1996; Giambanco and Di Gati 1997), until an appropriate constitutive model for analysis of masonry shear walls was developed by Lourenco and Rots (1997) to simulate/predict the ultimate strength and post-peak behavior of masonry. The Lourenco and Rots' model is a multi-surface composite interface model (CIM) that consists of three different failure criteria (failure surfaces), i.e., a Rankine failure criterion (tension cut-off criterion) for mode-I failure (opening in tension), a Mohr-Coulomb failure criterion for mode-II failure (in plane shearing or sliding), and a compression cap failure criterion for compression failure. The Rankine and the Mohr-Coulomb failure surfaces are coupled through internal softening parameters, whereas the Mohr-Coulomb and the compression cap failure surfaces are uncoupled. This multi-surface CIM has been used by many researchers to investigate the behavior of masonry structures (Oliveira and Lourenço 2004; Furukawa et al. 2010; Dolatshahi and Aref 2011; Tarque 2011; Miccoli et al. 2015).

Numerous interface element's constitutive models (based on numbers of failure surfaces, different failure criteria, and softening/hardening hypotheses) have been proposed to investigate the behavior of masonry by using the SMM approach. The simplest approach in defining an interface element's constitutive model is to adopt one failure surface to describe each of the three major failure mechanisms, i.e., tension, shear, and compression, (Lourenço 1996; Oliveira and Lourenço 2004; Chaimoon and Attard 2007; Minga et al. 2018). However, the use of multiple failure surfaces leads to singularity problems at the intersections between two of these surfaces (Abbo and Sloan 1995). Therefore, several constitutive models were developed with failure surfaces representing two (Lourenço 1994; Macorini and Izzuddin 2011) or three (Citto 2008; Bakeer 2009; Kumar et al. 2014b) failure mechanisms at a time. The usage of these more complex failure surfaces can introduce issues of robustness and may increase the computational cost of the constitutive model (Lourenço 1994).

This paper proposes a new interface element's constitutive model that is capable of simulating tension cracking, shear slipping, and compression failure for masonry analysis using the SMM approach. The proposed constitutive model is developed within the framework of non-associative elastoplastic materials with softening. It is noted here that other approaches could be used to improve the efficiency and robustness of masonry modeling based on the SMM approach, e.g., the plasticity-damage approach (Gambarotta and Lagomarsino 1997a, 1997b; Minga et al. 2018), the variational approach (Khisamitov and Meschke 2018), the damage approach (Greco et al. 2017; Khisamitov and Meschke 2018), and the elasto-viscoplastic modeling approach (Shing and Manzouri 2004; Tang et al. 2007). However, the consideration of these alternative approaches is beyond the scope of this study. The robustness and computational cost of the proposed constitutive model are compared to those of different constitutive models that have been widely used in the

literature to describe masonry behavior through a one-element test. In addition, the performance of the different constitutive models is investigated in terms of accuracy and computational cost by simulating an unreinforced masonry shear wall for which well-documented experimental results are available in the literature. Finally, conclusions are made based on the results obtained in the present study.

Research significance

This paper introduces a novel mechanical constitutive model for interface elements used in the context of the SMM approach for masonry structures. The proposed constitutive model achieves robustness, computational efficiency, and accuracy in modeling masonry structures under multi-axial stress conditions by (1) overcoming the singularity problem that arises from the interaction between the Mohr-Coulomb failure criterion and the Rankine failure criterion, and (2) using the strain hardening/softening hypothesis to improve the numerical robustness of the solution during the evolution of the yield surfaces. In addition, the proposed constitutive model is easily extendable to cyclic/hysteretic behavior. Therefore, the constitutive model developed here for interface elements can extend the usage of the SMM approach to investigate the behavior of masonry components and structures.

This paper also investigates the advantages and disadvantages of different constitutive models for interface elements when using the same integration scheme. This comparison provides useful information for further development of interface element's constitutive models to simulate the mechanical behavior of masonry and other quasi-brittle materials.

Proposed coupled tension-shear interface model (CTSIM)

Interface elements permit discontinuities in the displacement field, and their behavior can be described in terms of a relation between the traction, $\boldsymbol{\sigma}$, and relative displacements, $\boldsymbol{u}$, across the

interface. Thus, the generalized elastic behavior of the interface element's constitutive model can be written in standard form as

$$\boldsymbol{\sigma} = \boldsymbol{k} \cdot \boldsymbol{u} \tag{1}$$

where, for a 3D configuration, $\boldsymbol{\sigma} = \{\sigma, \tau_s, \tau_t\}^T$, $\boldsymbol{u} = \{u_n, u_s, u_t\}^T$, and $\boldsymbol{k} = \text{diag}[k_n, k_s, k_t]$, $\text{diag}[\bullet]$ denotes the diagonal matrix operator, n denotes the normal components, and s and t denote the shear components in two orthogonal directions. The component of the elastic stiffness matrix, $\boldsymbol{k}$, for the constitutive model in the SMM approach can be obtained from the properties of the masonry components (i.e., masonry units and mortar), and can be written as follows (Rots and Picavet 1997):

$$\frac{1}{k_n} = \left(\frac{h_m}{E_m} - \frac{h_m}{E_b} \right), \frac{1}{k_s} = \frac{1}{k_t} = \left(\frac{h_m}{G_m} - \frac{h_m}{G_b} \right) \tag{2}$$

where E_m and E_u are Young's modulus for mortar and masonry units, respectively; G_m and G_u denote the shear modulus for mortar and masonry units, respectively; and h_m is the thickness of the mortar joints. It is noted that Eq. (2) may significantly overestimate the elastic stiffness of the masonry joint's interface, particularly when the masonry units are weaker than the mortar or when the bond surface between mortar and units presents gaps (Rots and Picavet 1997; Chisari et al. 2018). Thus, several approaches have been proposed to obtain a better representation of the actual response of unreinforced masonry, e.g., by introducing a reduction factor in the calculation of the elastic stiffness based on Eq. (2) (Rots and Picavet 1997; Chaimoon and Attard 2007; da Porto et al. 2010), or by proposing more refined model parameter calibration strategies (Chisari et al. (2015).

The inelastic behavior of the proposed constitutive model for interface elements, referred to as coupled tension-shear interface model (CTSIM) hereafter, is defined by a convex composite failure

surface (shown in **Fig. 1**), which consists of a tension-shear failure criterion $F_1(\boldsymbol{\sigma}, \kappa_1, \kappa_2)$ and a compression cap failure criterion $F_2(\boldsymbol{\sigma}, \kappa_3)$, where κ_1, κ_2, and κ_3 are the scalar softening/ hardening parameters. The selection of this composite failure surface, which removes the singularity in the tension-shear region but not in the compression-shear region, is based on the fact the shear and tensile behaviors of mansonry are coupled while the compression and shear behaviors can be considered as uncoupled (Lourenço 1996). Thus, removing the singularity in the tension-shear region can reduce the computational cost of the interface element, whereas removing the singularity in the compression-shear region is not effective in reducing the computational cost of the interface element (Lourenço 1994). It is noteworthy that the specific form of $F_1(\boldsymbol{\sigma}, \kappa_1, \kappa_2)$ used in this study presents several novel characteristics when compared to other existing models, and has been used here for the first time in the context of interface elements for masonry modeled using the SMM approach.

Tension-shear failure criterion

A single hyperbolic surface is used for representing pressure-dependent shear failure and tensile cracking. The usage of this surface overcomes the singularity problem that occurs in multi-surfaces failure criteria, i.e., in the combination of the Mohr-Coulomb and Rankine failure criterion (Abbo and Sloan 1995) and it enables the proposed interface element's constitutive model to converge faster for larger load steps at the Gauss point level. The failure criterion originally proposed by Caballero et al. (2008) for concrete fracture problem is adopted here for the first time to describe the tension-shear yield surface, which is given as:

$$F_1(\boldsymbol{\sigma}, \kappa_1, \kappa_2) = -[C(\kappa_1, \kappa_2) - \sigma \cdot \tan\phi(\kappa_1, \kappa_2)] + \sqrt{\tau^2 + [C(\kappa_1, \kappa_2) - \bar{\sigma}_{f_t}(\kappa_1, \kappa_2) \cdot \tan\phi(\kappa_1, \kappa_2)]^2} \qquad (3)$$

where $\tau^2 = \tau_s^2 + \tau_t^2$, ϕ is the frictional angle, $\bar{\sigma}_{f_t}(\kappa_1, \kappa_2)$ is the tensile yield stress, and $C(\kappa_1, \kappa_2)$ is the cohesive yield stress. This hyperbolic failure criterion represents an improvement with

respect to other criteria described by quadratic terms (Caballero 2005; Citto 2008; Macorini and Izzuddin 2011), which consist of two hyperbolic branches, only one of which has physical meaning. Therefore, this modified yield function relaxes the requirement for small load steps at the Gauss point level, which otherwise would be needed to guarantee that the computed stress is associated with the correct branch of the hyperbolic surface (Caballero et al. 2008). A strain-softening hypothesis is considered for this failure criterion, in which the normal and shear plastic relative displacements jointly control the softening of both tensile and cohesive yield stresses. The tensile and cohesive yield stresses are implicitly coupled and softening in the tensile yield stress produces a proportional softening in the cohesive yield stress and vice versa. Thus, the rates of the scalar softening parameters are defined as follows by adapting the expressions originally derived in Lourenco (1996) to satisfy simultaneously the Mohr-Coulomb and Rankine failure criteria at their singularity point:

$$\dot{\kappa}_1 = \left\langle \dot{u}_n^p \right\rangle + \frac{G_f^I}{G_f^{II}} \cdot \frac{C_0}{f_t} \cdot \sqrt{\left|\dot{u}_s^p\right|^2 + \left|\dot{u}_t^p\right|^2} \tag{4}$$

$$\dot{\kappa}_2 = \frac{G_f^{II}}{G_f^I} \cdot \frac{f_t}{C_0} \cdot \left\langle \dot{u}_n^p \right\rangle + \sqrt{\left|\dot{u}_s^p\right|^2 + \left|\dot{u}_t^p\right|^2} \tag{5}$$

respectively, where f_t is the tensile strength; C_0 is the initial cohesion; G_f^I is the mode-I fracture energy; G_f^{II} is the mode-II fracture energy; u_n^p, u_s^p, and u_t^p denote the plastic relative displacements in the n, s and t directions, respectively; $\langle \bullet \rangle$ denotes the Macaulay brackets; and a superposed dot indicates differentiation with respect to (pseudo-)time. This form of the rates of the softening parameters allows their efficient computation when using a single smooth yield surface. In fact, the usage of the Macaulay brackets ensures that the softening parameters are affected by tensile stresses in the shear-tension region, whereas they are not affected by compression stresses in the

shear-compression region, consistently with the typical behavior of masonry joints (which are damaged by tension and shear stresses, but not by low compression stresses). The tensile yield stress $\bar{\sigma}_{f_t}(\kappa_1,\kappa_2)$ and cohesive yield stress $C(\kappa_1,\kappa_2)$ are defined as

$$\bar{\sigma}_{f_t}(\kappa_1,\kappa_2) = f_t \cdot \exp\left[-\sqrt{\left(\frac{f_t}{G_f^I}\cdot\kappa_1\right)^2 + \left(\frac{C_0}{G_f^{II}}\cdot\kappa_2\right)^2}\right] \tag{6}$$

$$C(\kappa_1,\kappa_2) = C_0 \cdot \exp\left[-\sqrt{\left(\frac{f_t}{G_f^I}\cdot\kappa_1\right)^2 + \left(\frac{C_0}{G_f^{II}}\cdot\kappa_2\right)^2}\right] \tag{7}$$

respectively. The exponential terms are defined so to ensure that the tensile and cohesive yield stresses evolve in a proportional fashion (i.e., the shape of the yield function remains the same during the analysis) and include the effects of both softening parameters. The softening of the friction angle is assumed proportional to the softening of the cohesive yield stress, i.e.

$$\tan\phi(\kappa_1,\kappa_2) = \tan\phi_r + \left(\tan\phi_0 - \tan\phi_r\right)\cdot\frac{C(\kappa_1,\kappa_2)}{C_0} \tag{8}$$

where ϕ_0 is the initial friction angle and ϕ_r is the residual friction angle. A non-associative formulation is assumed for the tension-shear failure criterion because the friction angle, ϕ, and the dilatancy angle, ψ, are generally considerably different for masonry (Atkinson et al. 1989; Van der Pluijm et al. 2000). The plastic potential function $Q_1(\boldsymbol{\sigma},\kappa_1,\kappa_2)$ is defined as (Caballero 2005):

$$Q_1(\boldsymbol{\sigma},\kappa_1,\kappa_2) = -[C_Q(\kappa_1,\kappa_2) - \sigma\cdot\tan\psi(\kappa_1,\kappa_2)]^2 + \tau^2 + [C_Q(\kappa_1,\kappa_2) - \bar{\sigma}_{f_t}(\kappa_1,\kappa_2)\cdot\tan\psi(\kappa_1,\kappa_2)]^2 \tag{9}$$

where $C_Q(\kappa_1,\kappa_2)$ is the apparent cohesive yield stress. The behavior of parameters C_Q and ψ are obtained by substituting C_Q and C_{Q0} to C and C_0, respectively, in Eq. (7), and, ψ_0 and ψ_r to ϕ, ϕ_0 and ϕ_r, respectively, in Eq. (8). The plastic potential function in Eq. (9) consists of quadratic terms and, thus, of two hyperbolic branches, similar to the failure yield criterion used,

e.g., in Caballero (2005), Macorini and Izzuddin (2011), and Citto (2008), in which the same functional form was employed for both yield criterion and plastic potential function. However, since for the proposed CTSIM the yield criterion functional form is different from that of the plastic potential function, the existance of a non-physically meaningful branch does not introduce convergence issues, because only the physically meaningful branch is actually used due to the constraints imposed by the consistency condition during the plastic-corrector step of the CTSIM's return mapping algorithm (Simo and Hughes 2006). The plastic potential function defined by Eq. (9) presents several computational advantages when compared to other existing expressions, e.g., the derivatives of the plastic potential function with respect to stress are simpler than those for the plastic potential function proposed in Caballero et al. (2008).

Compression cap failure criterion

The compression cap model used in the proposed constitutive model used here is described by an elliptical yield function originally introduced for orthotropic plasticity of soil materials (Schellekens 1992), which is given by

$$F_2(\boldsymbol{\sigma}, \kappa_3) = C_{nn} \cdot \sigma^2 + C_{ss} \cdot \tau^2 + C_n \cdot \sigma - \bar{\sigma}^2_{comp}(\kappa_3) \tag{10}$$

where C_{nn} and C_n are parameters that control the coordinates of the center of the compression cap failure surface, C_{ss} is a parameter that controls the width of the cap failure surface in the shear stress axis, and $\bar{\sigma}^2_{comp}(\kappa_3)$ is the compressive yield stress, which determines the width of the cap failure surface in the compressive stress axis. In the present study, the center of the cap failure surface is assumed to coincide with the origin of the $\sigma - \tau$ plane with $C_{nn} = 1$ and $C_n = 0$, in order to avoid the activation of this surface in the tension-shear region, which is controlled by the tension-shear failure criterion described in the previous subsection. A strain hardening/softening

hypothesis is introduced for the compressive yield stress, which describes the rate of the corresponding scalar softening parameter as

$$\dot{\kappa}_3 = \sqrt{\left(\dot{u}_n^p\right)^2 + \left(\dot{u}_s^p\right)^2 + \left(\dot{u}_t^p\right)^2} \tag{11}$$

and the compressive yield stress is defined as

$$\bar{\sigma}_{comp}(\kappa_3) = \begin{cases} \bar{\sigma}_0 + \left(\bar{\sigma}_p - \bar{\sigma}_0\right) \cdot \left(\dfrac{2\kappa_3}{\kappa_p} - \dfrac{\kappa_3^2}{\kappa_p^2} \right) & \text{if } \kappa_3 \le \kappa_p \\ \bar{\sigma}_p + \left(\bar{\sigma}_m - \bar{\sigma}_p\right) \cdot \left(\dfrac{\kappa_3 - \kappa_p}{\kappa_m - \kappa_p} \right)^2 & \text{if } \kappa_p < \kappa_3 \le \kappa_m \\ \bar{\sigma}_r + \left(\bar{\sigma}_m - \bar{\sigma}_r\right) \cdot \exp\left(m \cdot \dfrac{\kappa_3 - \kappa_m}{\bar{\sigma}_m - \bar{\sigma}_r} \right) & \text{if } \kappa_3 > \kappa_m \end{cases} \tag{12}$$

where $m = 2(\bar{\sigma}_m - \bar{\sigma}_p)/(\kappa_m - \kappa_p)$; $\bar{\sigma}_0$, $\bar{\sigma}_p$, $\bar{\sigma}_m$, and $\bar{\sigma}_r$ are initial (i.e., corresponding to the transition from linear to nonlinear behavior), peak, intermediate (i.e., corresponding to the inflection point in the softening branch), and residual compressive yield stress, respectively; and κ_p and κ_m denote the total plastic strain at peak and intermediate compressive yield stress. **Fig. 2** illustrates the evolution of the compressive yield stress, $\bar{\sigma}_{comp}$, as a function of the parameter κ_3. In Eq. (12), the first branch was taken from Lotfi and Shing (1991), whereas the second and third branches were taken from Lourenço (1996). An associative flow rule is assumed for the compression cap failure criterion, thus, $Q_2(\boldsymbol{\sigma}, \kappa_3) = F_2(\boldsymbol{\sigma}, \kappa_3)$.

The CTSIM has been implemented in the commercial finite element software package ABAQUS (Dassault Systémes 2013a) through an user-defined material subroutine (UMAT) written in FORTRAN (Metcalf et al. 2011) for an implicit integration scheme (Bathe 2006). The implicit backward Euler integration method (Simo and Hughes 2006) is used to integrate the different constitutive equations of the CTSIM, which leads to a system of nonlinear algebraic

equations. These nonlinear equations are solved monolithically with the local/global Newton-Raphson technique as described in Ottosen and Ristinmaa (2005), Caballero et al. (2008), and Macorini and Izzuddin (2011) which leads to a combined local and global solution strategy. In addition, the CTSIM is combined with an adaptive sub-stepping strategy to ensure convergence and accuracy of the final solution at both local and global levels (Pérez-Foguet et al. 2001; Caballero et al. 2008; Macorini and Izzuddin 2011).

Comparison of constitutive models using one-element test

In this section, the robustness, computational cost, and accuracy of the CTSIM are compared with three interface element's constitutive models that are available in the literature, namely the constitutive models proposed by Lourenco and Rots (1997), Macorini and Izzuddin (2011) and Citto (2008). **Fig. 3** shows the typical failure surfaces corresponding to each of these constitutive models and compares them with the failure surface corresponding to the CTSIM. These failure surfaces are plotted using the following values of the material parameters: $C = 0.35$ MPa, $\bar{\sigma}_{f_t} = 0.25$ MPa, $\bar{\sigma}_{comp} = 3.50$ MPa, and $\tan\phi = 0.65$. The Lourenco's model consists of three failure surfaces, as previously described in the Introduction section. The Macorini's model is defined by two hyperbolic failure surfaces (failure criteria), i.e., a tension-shear failure surface that represents Mode-I and Mode-II fracture, and a compression failure surface. Both failure surfaces shrink when the plastic work (which drives the softening of the material parameters) increases. The Citto's model is comprised of a single failure surface (failure criteria), which represents all three failure mechanisms of the interface element, i.e., Mode-I, Mode-II, and compression failure. The evolution of the hardening parameters is governed by a set of work hardening/softening rules and the rate of plastic work (Citto 2008). It is also observed that the CTSIM and Lourenco's model use the hypothesis of strain hardening for the evolution of the hardening/softening parameters;

whereas, the Macorini's and Citto's models use the hypothesis of work hardening. All these constitutive models were also implemented in the FE software ABAQUS (Dassault Systémes 2013a) by using a UMAT subroutine, similar to the implementation of the CTSIM, in order to provide a common platform for the comparison of these models with the CTSIM by removing the bias that could arise from the usage of different integration schemes.

One-element test

In the following section, the performance of the different models is assessed through a one-element test. A single zero-thickness interface element is subjected to thirteen different load paths defined by the angle $\theta = \arctan\left(u_\tau / u_n\right)$, where $u_\tau = \sqrt{u_s^2 + u_t^2}$ (as shown in **Fig. 4**), i.e., by considering a proportional increase of axial and shear relative displacements corresponding to θ = 0°, 15°, 30°, 45°, 60°, 75°, 90°, 105°, 120°, 135°, 150°, 165°, and 180°. The relative displacement magnitude was incremented from $|\boldsymbol{u}| = 0$ mm to $|\boldsymbol{u}| = 0.2$ mm using a displacement control analysis. Four different load step sizes were considered by dividing the final relative displacements into 5, 10, 50, and 100 equal increments (designated as N5, N10, N50, and N100 respectively). The material parameters corresponding to the joints of a shear wall described in Vermeltfoort and Raijmakers (1993a, 1993b) and given in

Table 1 and

Table 2 were used in these one-element tests. The adaptive sub-stepping algorithm was not activated in any of the considered constitutive models during these analyses to ensure a consistent (i.e., fixed) load step size for all constitutive models during each set of analyses. A total of 52 finite element response simulations (corresponding to 13 load paths each with four load step sizes) were

carried out for each constitutive model, and these simulations were performed in ABAQUS (Dassault Systémes 2013a) with one CPU on a computer having an Intel(R) Core(TM) i5-2400S CPU @ 2.50 GHz processor and 12.0 GB RAM.

For determining the accuracy of the constitutive models, a base load step size corresponding to 1,000 relative displacement increments (i.e., N1000 with $|\Delta \boldsymbol{u}| = 2\times10^{-4}$ mm) is used to compare the results of the one-element tests. This load step size is considered sufficiently small to serve as an accurate reference solution for estimating the percentage error, δ, which is evaluated through the expression (Simo and Taylor 1986):

$$\delta = \frac{\sqrt{\left(\boldsymbol{\sigma}_n - \boldsymbol{\sigma}_{exact}\right)^T \cdot \left(\boldsymbol{\sigma}_n - \boldsymbol{\sigma}_{exact}\right)}}{\sqrt{\boldsymbol{\sigma}_{exact}^T \cdot \boldsymbol{\sigma}_{exact}}} \times 100 \tag{13}$$

in which $\boldsymbol{\sigma}_n$ denotes the numerical traction response of the single interface element obtained by using different relative displacement increments, and $\boldsymbol{\sigma}_{exact}$ denotes the reference solution of the traction response corresponding to the same constitutive model used to evaluate $\boldsymbol{\sigma}_n$ with 1000 relative displacement increments (i.e., for N1000 load step sizes). The CPU time ratio (CTR) of the simulations for the different constitutive models with respect to the CPU time of the reference solution obtained using the CTSIM for each load path is also calculated. The results in terms of CTR and δ for the different constitutive models are reported in

Table 3 and **Table 4** for the tension-shear region (load paths θ = 0°, 15°, 30°, 45°, 60°, 75°, 90°) and compression-shear region (load paths θ = 105°, 120°, 135°, 150°, 165°, and 180°), respectively. Simulation results having percentage errors δ higher than 5% are identified by underlines in these tables. Some simulations did not converge to a solution for large (fixed) load step sizes and are identified by a hyphen. As expected, the presented results indicate that the δ increase for decreasing CTR along all load paths for all constitutive models.

Tension-shear region

In the tension-shear region, nine simulations (out of 28 simulations) did not converge for both Macorini's and Citto's models, whereas all simulations for the CTSIM and Lourenco's model reached convergence for all load step sizes. Among the converged simulations, 27 simulations converged with less than 5% errors for the CTSIM (i.e., only one simulation had δ larger than 5%), 25 simulations converged with less than 5% errors for the Lourenco's model (i.e., three simulations had δ larger than 5%), 17 simulations converged with less than 5% errors for the Macorini's model (i.e., two simulations had δ larger than 5% in addition to the nine simulations that did not converge), and 13 simulations converged with less than 5% errors for the Citto's model (i.e., six simulations had δ larger than 5% in addition to the nine simulations that did not converge). Considering only the converged cases, the CPU time used by the simulation based on the CTSIM is less than or equal to the CPU time corresponding to the Lourenco's, Macorini's, and Citto's models in 25 (out of 28), 17 (out of 19), and 12 (out of 19) simulations, respectively.

The results presented in

Table 3 for the tension-shear region indicate that the CTSIM is: (1) computationally robust for all load step sizes except for case N5 of load path $\theta = 90^{o}$, (2) generally more accurate and computationally robust than the other three constitutive models considered here, and (3) computationally efficient, since for all considered load paths it can provide accurate results with load step sizes that are larger than or equal to those needed for any other constitutive models.

In order to understand better the mechanical differences among the different models, iso-error maps (Simo and Taylor 1986; De Borst and Feenstra 1990; Fuschi et al. 1992) were developed for all four constitutive models at the point on the yield surfaces corresponding to load path $\theta = 36.13°$ (see **Fig. 5**). This point was selected as representative of the tension-shear region because

it corresponds to the singularity point between the Rankine and Mohr-Coulomb failure criteria in the Lourenco's model and, thus, can be used to illustrate the advantages of using a single surface failure criterion by eliminating the singularity in the tension-shear region. The iso-error maps plot the error defined in Eq. (13) as a function of the normalized increment of relative displacement in the axial direction, u_n, and in the shear direction, u_τ. The normalization parameter for each of these relative displacement increments corresponds to the elastic relative displacement associated with the initial yielding in each of the two directions, respectively. **Fig. 5**(a) through **5**(d) plot the iso-error maps for the CTSIM, Lourenco's, Macorini's, and Citto's models, respectively. The inset in each subfigure shows the location on the corresponding yield surface of the point selected as the origin of the iso-error map. The shaded region in each subfigure indicates the combinations of relative displacement increments for which the corresponding model cannot achieve convergence. It is observed that, within the range of normalized relative displacement increments considered here, the CTSIM is the only model that can always achieve convergence. The Lourenco's model does not converge within a region that corresponds approximately to $\Delta u_n / u_{ny} \geq 1$ and $\Delta u_\tau / u_{\tau y} \geq \Delta u_n / u_{ny}$. This result was first qualitatively observed in Lourenço (1994) and is due both to the presence of a singularity in the yield surface and to the heuristic (i.e., trial-and-error) approach adopted in the Lourenco's model to identify the active yield surface(s), which cannot guarantee convergence of the analysis for large load step sizes (Lourenço 1994). The Macorini's and Citto's models also present a region of non-convergence, corresponding approximately to $\Delta u_n / u_{ny} \geq 2$ and $\Delta u_n / u_{ny} \geq 3$, respectively. This non-convergence region for these two models is due to the presence of a non-physically meaningful branch of the yield surface having a quadratic functional form, as previously discussed. In particular, the convergence of these models is impaired as soon as the imposed relative displacement increment intercepts the non-physically

meaningful branch of the corresponding yield surface. It is observed that, when the models converge, the magnitude of the errors is smallest for the Lourenco's model (i.e., less than 0.01%), followed by the CTSIM (i.e., less than or equal to approximately 2%), and then by the Macorini's and Citto's models (i.e., less than 10%). These error's magnitudes increase with the complexity of the functional form used for the corresponding yield surfaces (i.e., the Lourenco's model is represented by linear yield functions, which correspond to the simplest functional form and the smallest percentage errors). The errors also depend on the hardening/softening hypothesis used in each model (i.e., the Macorini's and Citto's models use a work hardening/softening hypothesis, which negatively affects the accuracy of their solutions when compared with the results obtained using the CTSIM and Lourenco's model, which adopt a strain hardening/softening hypothesis). Finally, it is also observed that the percentage error for all models is more sensitive to the size of the relative displacement increments in the axial direction than to that of the relative displacement increments in the shear direction. Based on these results, it is concluded that the CTSIM provides the best compromise between accuracy and robustness in the tension-shear region among all models considered in this study.

Compression-shear region

In the compression-shear region, two simulations (out of 24 simulations) did not converge for both Macorini's and Citto's models, whereas all simulations for the CTSIM and Lourenco's model reached convergence. Among the converged simulations, 19 simulations converged with less than 5% errors for the CTSIM and Lourenco's model (i.e., five simulations had δ larger than 5%), 18 simulations converged with less than 5% errors for the Macorini's model (i.e., four simulations had δ larger than 5% in addition to the two simulations that did not converge), and 12 simulations converged with less than 5% errors for the Citto's model (i.e., nine simulations had δ larger than

5% in addition to the three simulations that did not converge). Considering only the converged cases, the CPU time used by the simulation based on the CTSIM is less than or equal to the CPU time corresponding to the Lourenco's, Macorini's, and Citto's models in 21 (out of 24), 16 (out of 22), and 18 (out of 22).

The results presented in **Table 4** indicate that the performance of CTSIM in the compression-shear region is practically identical to that of the Lourenco's model since both models use the same compression cap model for representing the compression failure. These models are: (1) computationally robust for all load step sizes except for the N5 (load paths θ = 120º, 135º, 150º, 165º, and 180º) and N10 (load paths θ = 150º and 165º); (2) more accurate and computationally robust than the Macorini's, and Citto's models; and (3) computationally efficient, since both models provide accurate results with load step sizes that are larger than or equal to those for the Macorini's and Citto's models.

Discussion of one-element test results

The different performance of the constitutive models cosidered here can be more easily interpreted by analyzing the properties of the integration algorithm (i.e., the elastic predictor-plastic corrector strategy with local/global Newton-Raphson integration) and its interaction with the constitutive models' equations. During the plastic-corrector step, different sets of equations are solved in the different constitutive models depending upon which failure surface(s) is(are) violated, leading to different sizes of the Jacobian matrix that needs to be inverted. The size of this Jacobian matrix and the complexity of each Jacobian component both contribute towards the computational cost and accuracy of the different constitutive models in the different regions (i.e., tension, shear, and compression cap regions). For the CTSIM, three different cases can be encountered during the plastic-corrector step: (1) violation of the tension-shear failure surface,

which involves a 6×6 Jacobian matrix (see Eq. (14) in Appendix); (2) violation of the compression cap failure surface, which involves a 5×5 Jacobian matrix (see Eq. (15) in Appendix); and (3) violation of both failure surfaces, which involves an 8×8 Jacobian matrix (see Eq. (16) in Appendix). **Fig. 6** illustrates the size of the Jacobian matrix used in the different regions of the different constitutive models.

The CTSIM is at least as efficient as the Lourenco's model along load paths θ = 0º, 15º, 30º, 45º, and 60º. In this region, the return mapping algorithm for the Lourenco's model requires inverting a 3×3, 5×5, and/or 7×7 Jacobian matrix, depending on which failure surface(s) is(are) violated, whereas the the CTSIM requires the inversion of a 6×6 Jacobian matrix. However, the Jacobian matrix for the Lourenco's model mainly assumes a 7×7 dimension because, in most of the cases, both the Rankine and the Mohr-Coulomb failure surfaces are simultaneously violated, generally for large load steps or even for small load steps after the failure surfaces have experienced softening of their scalar parameters. The accuracy of the results obtained using the Lourenco's model is very similar or slightly lower than the accuracy of the CTSIM's results for load paths 15º, 30º, 45º, and 60º since the Lourenco's model requires the solution of a multi-surface plasticity problem (with a singularity located along the load path θ = 33.02º for the specific problem considered in this study), whereas the CTSIM uses a single surface in the same region. For load paths θ = 75º and 90º, the Lourenco's model is slightly more efficient than the CTSIM because the Jacobian matrix has dimensions 5×5 for the Lourenco's model and 6×6 for the CTSIM. However, the CTSIM is consistently more accurate than the Lourenco's model along these load paths, particularly for large load step sizes. In the shear-tension region, the Macorini's and the Citto's models are very similar, because they use the same equation to define the failure surface and the hypothesis of work hardening. When compared to the CTSIM, the Macorini's and Citto's

model perform poorly for load paths with small angles, i.e., $\theta \leq 60^{o}$. These two models perform better for load paths $\theta = 75^{o}$ and 90^{o}, and Citto's model is the most efficient and accurate model for $\theta = 90^{o}$.

In the compression-shear region, both the CTSIM and Lourenco's model have a similar efficient and accurate behaviour, with the exception of cases corresponding to large load step sizes. This is due to the fact that in this region the two models use the same failure criteria. In the compression-shear region, the Macorini's and Citto's model are very different from each other and from the other constitutive models. In general, the Macorini's model is generally more efficient than the CTSIM and Lourenco's model for small load step sizes, but is less accurate (or lacks convergence) for large load step sizes. The Citto's model generally performs poorly, both in terms of efficiency and accuracy. The efficiency of the Macorini's model for small load step sizes can be attributed to its evolution model for the compressive yield stress, which assumes a linear behavior up to the peak compressive yield stress, after which softening of the compressive yield stress takes place (Macorini and Izzuddin 2011). By contrast, the CTSIM and Lourenco's model assume a linear behavior only up to an initial compressive yield stress that is significantly lower than the peak compressive yield stress (e.g., approximately 1/3 of it for quasi-brittle materials (Bakeer 2009)), which is followed by hardening till the peak compressive yield stress and by softening afterward (see **Fig. 2** and Eq. (12)). In addition, it appears that the lower accuracy of the Macorini's and Citto's models may be related to their use of the work hardening hypothesis, in contrast with the CTSIM and Lourenco's model that use the hypothesis of strain hardening. In particular, for the specific problem considered in this paper of interface element's constitutive models for masonry analysis based on the SMM approach, the hypothesis of strain hardening/softening appears to improve the robustness of the numerical response for yield surfaces

that evolve for increasing plastic deformation, as assumed by the softening plasticity framework adopted in this study.

Constitutive model comparison using masonry shear wall experimental data

The performance of the proposed CTSIM is compared with the other constitutive models considered in this study through the numerical response analysis of an unreinforced masonry shear wall for which experimental data are available in Vermeltfoort and Raijmakers (1993a, 1993b). The numerical analyses were performed for all constitutive models using the FE software ABAQUS (Dassault Systémes 2013a).

The masonry shear wall consisted of a pier with a width to height ratio approximately equal to one, i.e., with dimensions 990 mm × 1000 mm, as shown in **Fig. 7**(a). The wall was built using wire cut solid clay blocks of dimensions 210 mm × 52 mm × 100 mm and mortar layers of thickness equal to 10 mm, and consisted of 18 courses of blocks, two of which (the bottom and top ones) were clamped to steel beams that were used to transfer the lateral load to the system, as shown in **Fig. 7**(a). The mortar was prepared with one part of cement, two parts of lime, and nine parts of sand. The experimental test involved a uniformly distributed normal pressure ($p = 0.30\ \text{MPa}$), followed by a monotonically increasing horizontal loading phase, in which a horizontal displacement Δ was applied quasi-statically to the top of the wall through a steel beam while keeping the bottom boundary fixed horizontally. The material properties of blocks and mortar were obtained from experimental results of tension, shear, and compression tests reported in the literature Vermeltfoort and Raijmakers (1993a, 1993b) and are the same as those reported in

Table 1 (elastic properties) and

Table 2 (inelastic properties).

Definition of FE models for unreinforced masonry shear wall

The SMM approach with elastic masonry units and non-linear joints was adopted here for the FE modeling of the unreinforced masonry shear wall described above. Plane stress conditions were assumed, and geometric non-linearity (i.e., large strains and large displacements (Dassault Systèmes 2013b)) was also included in the simulation of the FE models. The FE model consisted a set of elastic masonry units bonded by potential crack, potential slip, and crushing planes at joints, see **Fig. 7**(b). For modelling cracking of the masonry units, a potential crack was placed vertically in the middle of each unit as shown in **Fig. 7**(b). All the degrees of freedoms are restrained at the bottom of the FE model, and a monotonically increasing horizontal displacement is applied on the side of the top course of the FE model while keeping the top edge of the FE model vertically fixed, see **Fig. 7**. A general procedure for static loading based on an incremental-iterative globally-convergent Newton-Raphson method with the line search technique was used in ABAQUS (Dassault Systémes 2013a) for solving the nonlinear system of equilibrium equations for the different FE models (Dassault Systèmes 2013b). In addition, an automatic load step increment technique was adopted for efficient and robust simulation of the response of the different FE models with initial, minimum, and maximum normalized increment sizes equal to 1×10^{-4}, 1×10^{-9}, 5×10^{-4}, respectively.

In the FE models of the masonry shear wall, the masonry units were modeled using a 4-node bilinear plane stress quadrilateral element with reduced integration and hourglass control (CPS4R element (Dassault Systèmes 2013b)), and the joints and potential cracks were modeled by using a 4-node two-dimensional cohesive element (CPS4R element (Dassault Systèmes 2013b)). A mesh sensitivity analysis of the FE Model was performed to ensure a good compromise between

accuracy and computational costs for all the constitutive models. The mesh used in this study consisted of six interface elements employed for each bed joints (i.e., three interface elements for the bed joint of each half masonry unit), two interface elements employed for each head joint and for potential vertical cracks, and six CPS4R elements for each half masonry unit. One FE model was built for each of the constitutive models considered in this study, i.e., CTSIM, Lourenco's, Macorini's, and Citto's models. The adaptive sub-stepping algorithm was activated for all considered constitutive models to achieve maximum computational efficiency in all FE analyses. It should be noted here that the behavior of the potential vertical cracks did not include the compression failure mechanism. Thus, the compression failure surface of the CTSIM, Lourenco's model, and Macorini's model was deactivated for the interface element of potential vertical cracks, and a high 'dummy' value in the Citto's model was used for the compressive yield stress to avoid activation of the failure surface in the compression region of this constitutive model.

Comparison of FE responses and experimental data

The comparison of the experimental load-displacement curves with their numerical counterparts for all constitutive models is shown in **Fig. 8**. The FE response results obtained using any of the interface element's constitutive models considered in this study are in very good agreement with the experimental behavior, with a ratio of the numerically simulated peak load over the average experimental peak load equal to 1.04, 1.01, 1.10, and 0.98 for the CTSIM, Lourenco's, Macorini's, and Citto's models, respectively. The deformed shape and the minimum principal stress distribution (corresponding to the maximum compressive stress) at an applied top horizontal displacement $\Delta = 4$ mm (i.e., the maximum displacement recorded in the experimental tests) of the FE analyses using different constitutive models are presented in **Fig. 9**. For the sake of visualization, the interface elements are represented by white empty spaces in this figure so that

highly plasticized interface elements appear as openings between masonry units. The stress distributions of the shear wall FE models corresponding to the different constitutive models were very similar. In addition, the crack patterns were also similar to those observed experimentally for all FE models, except for that corresponding to the Citto's model. During the application of the monotonically increasing horizontal load, horizontal tensile cracks developed at the bottom and top of the wall, particularly in the bed joint at an early loading stage, followed by the formation of a diagonal stepped crack due to a combined tension-shear failure of the joints. For large horizontal load levels, the diagonal stepped crack was followed by crushing of the toes of the masonry and tensile cracking within the masonry units, leading to the overall failure of the masonry wall. The cracking of the masonry units is significant for all constitutive models except for the Citto's model, in which the behavior of the potential vertical crack within a unit is more ductile than for the other constitutive models, leading to smaller crack's openings. This behavior is due to the use of a high 'dummy' value for the compressive yield stress of cracks within the masonry units, which is required to avoid the activation of the compressive failure surface in the Citto's model. In fact, while for the CTSIM, Lourenco's, and Macorini's models the compressive failure surface is independent of the tension-shear behavior, a change of the compressive yield stress in the Citto's model affects also the shape of the failure surface in the tension-shear region. This shape change deteriorates the capability of the Citto's model to simulate the brittle cracking of masonry units.

Assessment of computational cost

The FE models corresponding to the different constitutive models were also compared in terms of computational cost. In particular,

Table 5 reports the number of increments, cutbacks (reduction of load/displacement increment size when the iterative global solution algorithm cannot converge within a specified number of

iterations), and total iterations (Dassault Systèmes 2013b), as well as the CPU time ratios (CTR) corresponding to the FE analyses for each of the considered constitutive models. The CTRs were calculated with respect to the total CPU time corresponding to the FE analysis using the CTSIM, which was assumed as a reference with CTR = 1.00. The FE analysis based on the CTSIM took 9.53 hours of CPU time using an Intel(R) Core(TM) i5-2400S CPU @ 2.50 GHz processor and 12.0 GB RAM. It is noteworthy that the FE analysis using the CTSIM was found to be the least computationally expensive one among those considered in this study. The second most computationally efficient model was the Macorini's model with CTR = 1.22, followed by the Lourenco's model (CTR = 1.37) and the Citto's model (CTR = 1.48). Moreover, the CTSIM completed the simulation with the smallest numbers of increments, cutbacks, and total iterations. This result indicates that the CTSIM can allow FE simulation of the masonry shear wall with larger load steps than those corresponding to the other interface element's constitutive models, which explains the lower computational cost of the proposed constitutive model.

Table 6 reports the number of the local iterations corresponding to the different regions of constitutive models during the FE simulations of the benchmark masonry shear wall. It is observed that the CTSIM requires the least number of local iterations, i.e., 21.15 million, followed by the Macorini's (24.77 million), Lourenco's (27.68 million), and Citto's models (29.81 million).

The FE simulation with the CTSIM requires 17.96 local iterations (out of 21.15 million) occurring in the tension and shear failure region, which corresponds to a 6×6 Jacobian matrix. For the Lourenco's model, 24.58 million local iterations (out of 27.68 million) occur in the failure region. These local iterations are associated with three different failure conditions, i.e.: (1) violation of the Rankine failure criterion that requires the inversion of a 3×3 Jacobian matrix (0.52

million iterations); (2) violation of the Mohr-Coulomb failure criterion that requires the inversion of a 5×5 Jacobian matrix (18.47 million iterations); and (3) violation of both failure criteria simultaneously (T-S corner), which requires the inversion of a 7×7 Jacobian matrix (5.59 million iterations). By contrast, Thus, by comparing the FE simulations with the CTSIM and the Lourenco's model, it is observed that the use of a smooth failure surface instead of the two different failure surfaces (the Rankine and Mohr-Coulomb failure surfaces) results in 6.62 million fewer local iterations. Even though the computational cost associated with each local iteration for the two constitutive models is different (generally lower for the Lourenco's model), the CTSIM results in lower CPU times because of the significantly smaller number of iterations required. Therefore, it can be concluded that the use of smooth failure surface to describe the shear and tension failure region results in a more computationally efficient interface element's constitutive model. Furthermore, the FE simulation with the Macorini's model requires 24.42 million local iterations violating the tension and shear failure criterion, which is 6.46 million iterations more (approximately 35.97%) than the corresponding total local iterations for the CTSIM. In addition, the FE simulation with the Macorini's model required a comparatively higher number of global increments (approximately 33.60% higher) when compared with the CTSIM, as reported in

Table 5. The higher number of local iteration and global increments may be due to the fact that the Macorini's model requires smaller load step sizes to achieve the same accuracy of the CTSIM, as shown by the results reported for the one-element test.

In the compression cap failure region, the FE simulations of the masonry shear wall with the CTSIM and Lourenco's model results in 3.19 million and 3.10 million local iterations, respectively, which require the inversion of a 5×5 Jacobian matrix. Thus, the Lourenco's model is slightly more efficient than the CTSIM in the compression cap failure region. The Macorini's

model requires only 0.35 million local iterations that correspond to violating the compression failure surface. This difference in the number of local iterations when compared to the CTSIM and Lourenco's models is mainly due to the different assumptions for the evolution of the compressive yield stress and the different values for the initial compressive yield stress. In fact, these different assumptions result in the Macorini's model exhibiting linear elastic behavior for a much wider range of strains and stresses when compared to the CTSIM and Lourenco's model.

The FE simulation of the masonry shear wall with the Citto's model results in the largest number of local iteration, i.e., 26.81 million local iterations, compared to the other constitutive models. Thus, the Citto's model is the least efficient model among those considered in this study for simulating the response of this masonry shear wall. This result is due to: (1) the lower accuracy in normal and shear stress evaluations for a given load/displacement step size (as shown by the results reported for the one-element test); (2) the larger size of the Jacobian matrix (10×10) that needs to be inverted in the local iterations; (3) the more complex equation used for representation of the single failure surface. The comparison of the computational costs of the FE simulations corresponding to the different constitutive models considered in this study (i.e., the CTSIM, Lourenco's model, Macorini's model, and the Citto's model) indicate that the use of single failure surface for all failure modes decreases the overall computational efficiency of the interface element's constitutive model.

Conclusions

A new interface element's constitutive model, referred to as coupled tension-shear interface model (CTSIM), is proposed in this paper for finite element (FE) analysis of masonry using the simplified micro-modeling approach. This new model is capable of simulating tension cracking, shear slipping, and compression failure and is defined by a convex composite failure surface

consisting of a tension-shear failure criterion and a compression cap failure criterion. The constitutive model is implemented in the FE software ABAQUS through a user-defined material subroutine. The different constitutive equations of the CTSIM are integrated using the implicit backward Euler integration method, and the integrated equations are solved monolithically with the local/global Newton-Raphson technique, which leads to a combined local and global solution strategy. Moreover, the CTSIM is combined with an adaptive sub-stepping strategy to ensure convergence and accuracy of the final solution for larger load step sizes.

The performance of the CTSIM is assessed through a series of one-element tests and through the comparison of FE response simulation and experimental results for an unreinforced shear wall. Furthermore, the robustness, computational cost, and accuracy of the CTSIM are also compared with three constitutive models that are available in the literature, i.e., the Lourenco's, Macorini's and Citto's models. The comparison of one-element test's results shows that the CTSIM is at least as efficient as and generally more robust than the other constitutive models for varying load step sizes and load paths. The comparison of the FE results for the masonry shear wall indicates that the CTSIM is more efficient than and at least as accurate as the other constitutive models. Moreover, it is observed that: (1) the use of a single failure surface for mode-I and mode-II failure can improve the computational efficiency and robustness of the constitutive model when compared to constitutive models that use two separate failure surfaces; (2) the use of a single failure surface for all failure mechanisms has negative effects on the computational efficiency and robustness of the constitutive model when compared to constitutive models that use multi-surface criteria; and (3) constitutive models based on the hypothesis of strain hardening seem to be more efficient and robust than those based on the hypothesis of work hardening.

Appendix: Integration scheme for constitutive equations

The local/global Newton-Raphson strategy (Ottosen and Ristinmaa 2005; Caballero et al. 2008; Macorini and Izzuddin 2011) is used to solve the nonlinear system of algebraic equations obtained from the implicit backward Euler integration (Simo and Hughes 2006) of the CTSIM. This integration procedure leads to a set of algebraic-incremental equations that are solved using an elastic predictor-plastic corrector approach. The plastic correction step is performed when the trial stress violates at least one failure criteria (failure surfaces) and consists in an iteration process that requires: (1) evaluating the residuals of the non-linear constitutive equations, (2) evaluating the Jacobian of the residuals, (3) solving the set of algebraic equations to obtain the increments of the independent variables, (4) evaluating the updated residuals and repeating the iteration until these residuals become smaller than a specified tolerance. Three different cases can occur in the plastic correction step: (1) violation of the tension-shear failure criterion, (2) violation of the compression cap failure criterion, and (3) violation of both tension-shear and compression cap failure criteria. The Jacobian of the residuals for these three cases are:

1. Violation of the tension-shear failure criterion, with independent variables $\boldsymbol{\sigma}$, κ_1, κ_2, and $\Delta\lambda_1$:

$$\boldsymbol{J}\left(\boldsymbol{\sigma},\kappa_1,\kappa_2,\Delta\lambda_1\right)=\begin{bmatrix} \boldsymbol{I}_3+\boldsymbol{k}\cdot\Delta\lambda_1\cdot\dfrac{\partial^2 Q_1}{\partial\boldsymbol{\sigma}^2} & \boldsymbol{k}\cdot\Delta\lambda_1\cdot\dfrac{\partial^2 Q_1}{\partial\kappa_1\partial\boldsymbol{\sigma}} & \boldsymbol{k}\cdot\Delta\lambda_1\cdot\dfrac{\partial^2 Q_1}{\partial\kappa_2\partial\boldsymbol{\sigma}} & \boldsymbol{k}\cdot\dfrac{\partial Q_1}{\partial\boldsymbol{\sigma}} \\ -\dfrac{\partial\Delta\kappa_1}{\partial\boldsymbol{\sigma}} & 1-\dfrac{\partial\Delta\kappa_1}{\partial\kappa_1} & -\dfrac{\partial\Delta\kappa_1}{\partial\kappa_2} & -\dfrac{\partial\Delta\kappa_1}{\partial\lambda_1} \\ -\dfrac{\partial\Delta\kappa_2}{\partial\boldsymbol{\sigma}} & -\dfrac{\partial\Delta\kappa_2}{\partial\kappa_1} & 1-\dfrac{\partial\Delta\kappa_2}{\partial\kappa_2} & -\dfrac{\partial\Delta\kappa_2}{\partial\lambda_1} \\ -\dfrac{\partial F_1}{\partial\boldsymbol{\sigma}} & \dfrac{\partial F_1}{\partial\kappa_1} & \dfrac{\partial F_1}{\partial\kappa_2} & 0 \end{bmatrix}_{6\times 6} \tag{14}$$

where $\boldsymbol{I}_3$ represents the 3×3 identity matrix and $\Delta\lambda_1$ denotes the increment of the plastic multiplier for the tension-shear failure surface $F_1(\boldsymbol{\sigma},\kappa_1,\kappa_2)$.

2. Violation of the compression cap failure criterion, with independent variables $\boldsymbol{\sigma}$, κ_3, and $\Delta\lambda_2$:

$$\boldsymbol{J}\left(\boldsymbol{\sigma},\kappa_3,\Delta\lambda_2\right)=\begin{bmatrix} \boldsymbol{I}_3+\boldsymbol{k}\cdot\Delta\lambda_2\cdot\dfrac{\partial^2 F_2}{\partial\boldsymbol{\sigma}^2} & \boldsymbol{k}\cdot\Delta\lambda_2\cdot\dfrac{\partial^2 F_2}{\partial\kappa_3\partial\boldsymbol{\sigma}} & \boldsymbol{k}\cdot\dfrac{\partial F_2}{\partial\boldsymbol{\sigma}} \\ -\dfrac{\partial\Delta\kappa_3}{\partial\boldsymbol{\sigma}} & 1-\dfrac{\partial\Delta\kappa_3}{\partial\kappa_3} & -\dfrac{\partial\Delta\kappa_3}{\partial\lambda_2} \\ -\dfrac{\partial F_2}{\partial\boldsymbol{\sigma}} & \dfrac{\partial F_2}{\partial\kappa_3} & 0 \end{bmatrix}_{5\times5} \tag{15}$$

where $\Delta\lambda_2$ denotes the increment of the plastic multiplier for the compression cap failure surface $F_2(\boldsymbol{\sigma},\kappa_3)$.

3. Violation of both tension-shear and compression cap failure criteria (S-C corner), with independent variables $\boldsymbol{\sigma}$, κ_1, κ_2, κ_3, $\Delta\lambda_1$ and $\Delta\lambda_2$:

$$\boldsymbol{J}\left(\boldsymbol{\sigma},\boldsymbol{\kappa},\Delta\lambda_1,\Delta\lambda_2\right)=\begin{bmatrix} \boldsymbol{I}_3+\boldsymbol{k}\cdot\Delta\lambda_1\cdot\dfrac{\partial^2 Q_1}{\partial\boldsymbol{\sigma}^2}+\boldsymbol{k}\cdot\Delta\lambda_2\cdot\dfrac{\partial^2 F_2}{\partial\boldsymbol{\sigma}^2} & \boldsymbol{k}\cdot\Delta\lambda_1\cdot\dfrac{\partial^2 Q_1}{\partial\boldsymbol{\kappa}\,\partial\boldsymbol{\sigma}}+\boldsymbol{k}\cdot\Delta\lambda_2\cdot\dfrac{\partial^2 F_2}{\partial\boldsymbol{\kappa}\,\partial\boldsymbol{\sigma}} & \boldsymbol{k}\cdot\dfrac{\partial Q_1}{\partial\boldsymbol{\sigma}} & \boldsymbol{k}\dfrac{\partial F_2}{\partial\boldsymbol{\sigma}} \\ -\dfrac{\partial\Delta\boldsymbol{\kappa}}{\partial\boldsymbol{\sigma}} & \boldsymbol{I}_3-\dfrac{\partial\Delta\boldsymbol{\kappa}}{\partial\boldsymbol{\kappa}} & -\dfrac{\partial\Delta\boldsymbol{\kappa}}{\partial\lambda_1} & -\dfrac{\partial\Delta\boldsymbol{\kappa}}{\partial\lambda_2} \\ -\dfrac{\partial F_1}{\partial\boldsymbol{\sigma}} & \dfrac{\partial F_1}{\partial\boldsymbol{\kappa}} & 0 & 0 \\ -\dfrac{\partial F_2}{\partial\boldsymbol{\sigma}} & \dfrac{\partial F_2}{\partial\boldsymbol{\kappa}} & 0 & 0 \end{bmatrix}_{8\times8} \tag{16}$$

where $\boldsymbol{\kappa}=\{\kappa_1,\kappa_2,\kappa_3\}^T$. Note that some of the terms in Eqs. (14), (15), and (16) are matrices or vectors.

Acknowledgments

Partial support for this research by the Louisiana Board of Regents through the Economic Development Assistantship Program, and by the National Science Foundation through award CMMI #1537078 is gratefully acknowledged. Any opinions, findings, conclusions, or recommendations expressed in this publication are those of the writers and do not necessarily reflect the views of the sponsoring agencies.

References

Abbo, A., and Sloan, S. (1995). "A smooth hyperbolic approximation to the Mohr-Coulomb yield criterion." *Computers & Structures*, 54(3), 427-441.

Andreaus, U. (1996). "Failure criteria for masonry panels under in-plane loading." *Journal of Structural Engineering*, 122(1), 37-46.

Aref, A. J., and Dolatshahi, K. M. (2013). "A three-dimensional cyclic meso-scale numerical procedure for simulation of unreinforced masonry structures." *Computers & Structures*, 120, 9-23.

Atkinson, R., Amadei, B., Saeb, S., and Sture, S. (1989). "Response of masonry bed joints in direct shear." *Journal of Structural Engineering*, 115(9), 2276-2296.

Bakeer, T. T. (2009). *Collapse analysis of masonry structures under earthquake actions*, TU Dresden, Dresden, Germany.

Bathe, K.-J. (2006). *Finite element procedures*, Klaus-Jurgen Bathe, Watertown, MA.

Caballero, A. (2005). "3D meso-mechanical numerical analysis of concrete fracture using interface elements." PhD dissertation, Polytechnic University of Catalonia, Barcelona, Spain.

Caballero, A., Willam, K., and Carol, I. (2008). "Consistent tangent formulation for 3D interface modeling of cracking/fracture in quasi-brittle materials." *Computer Methods in Applied Mechanics and Engineering*, 197(33), 2804-2822.

Chaimoon, K., and Attard, M. M. (2007). "Modeling of unreinforced masonry walls under shear and compression." *Engineering Structures*, 29(9), 2056-2068.

Chisari, C., Macorini, L., Amadio, C., and Izzuddin, B. (2015). "An inverse analysis procedure for material parameter identification of mortar joints in unreinforced masonry." *Computers & Structures*, 155, 97-105.

Chisari, C., Macorini, L., Amadio, C., and Izzuddin, B. A. (2018). "Identification of mesoscale model parameters for brick-masonry." *International Journal of Solids and Structures*, 146, 224-240.

Citto, C. (2008). "Two-dimensional interface model applied to masonry structures." MS thesis, University of Colorado Boulder.

Cuellar-Azcarate, M. C. (2016). "Engineered earthen masonry structures for extreme wind loads." PhD dissertation, University of South Carolina, Columbia.

da Porto, F., Guidi, G., Garbin, E., and Modena, C. (2010). "In-plane behavior of clay masonry walls: experimental testing and finite-element modeling." *Journal of structural engineering*, 136(11), 1379-1392.

Dassault Systémes (2013a). "Abaqus 6.13 computer software." Dassault Systémes, Waltham.

Dassault Systèmes (2013b). "Abaqus 6.13 documentation." *Abaqus analysis user's guide,* Providence, RI.

De Borst, R., and Feenstra, P. H. (1990). "Studies in anisotropic plasticity with reference to the Hill criterion." *International journal for numerical methods in engineering*, 29(2), 315-336.

Dhanasekar, M., Kleeman, P. W., and Page, A. W. (1985). "Biaxial stress-strain relations for brick masonry." *Journal of Structural Engineering*, 111(5), 1085-1100.

Dolatshahi, K. M., and Aref, A. J. (2011). "Two-dimensional computational framework of meso-scale rigid and line interface elements for masonry structures." *Engineering Structures*, 33(12), 3657-3667.

Furukawa, A., Spence, R., Ohta, Y., and So, E. (2010). "Analytical study on vulnerability functions for casualty estimation in the collapse of adobe buildings induced by earthquake." *Bulletin of Earthquake Engineering*, 8(2), 451-479.

Fuschi, P., Perić, D., and Owen, D. (1992). "Studies on generalized midpoint integration in rate-independent plasticity with reference to plane stress J2-flow theory." *Computers & Structures*, 43(6), 1117-1133.

Gambarotta, L., and Lagomarsino, S. (1997a). "Damage models for the seismic response of brick masonry shear walls. Part II: The continuum model and its applications." *Earthquake Engineering and Structural Dynamics*, 26(4), 441-462.

Gambarotta, L., and Lagomarsino, S. (1997b). "Damage models for the seismic response of brick masonry shear walls. Part I: The mortar joint model and its applications." *Earthquake Engineering and Structural Dynamics*, 26(4), 423-439.

Giambanco, G., Rizzo, S., and Spallino, R. (2001). "Numerical analysis of masonry structures via interface models." *Computer Methods in Applied Mechanics and Engineering*, 190(49), 6493-6511.

Goodman, R. E., Taylor, R. L., and Brekke, T. L. (1968). "A model for the mechanics of jointed rocks." *Journal of the Soil Mechanics and Foundations Division*, 94(3), 637-660.

Greco, F., Leonetti, L., Luciano, R., and Trovalusci, P. (2017). "Multiscale failure analysis of periodic masonry structures with traditional and fiber-reinforced mortar joints." *Composites Part B: Engineering*, 118, 75-95.

Khisamitov, I., and Meschke, G. (2018). "Variational approach to interface element modeling of brittle fracture propagation." *Computer Methods in Applied Mechanics and Engineering*, 328, 452-476.

Kumar, N., Rajagopal, A., and Pandey, M. (2014a). "Plasticity based approach for failure modelling of unreinforced masonry." *Engineering Structures*, 80, 40-52.

Kumar, N., Rajagopal, A., and Pandey, M. (2014b). "A rate independent cohesive zone model for modeling failure in quasi-brittle materials." *Mechanics of Advanced Materials and Structures*, 22(8), 681-696.

Lotfi, H. R., and Shing, P. B. (1991). "An appraisal of smeared crack models for masonry shear wall analysis." *Computers & Structures*, 41(3), 413-425.

Lotfi, H. R., and Shing, P. B. (1994). "Interface model applied to fracture of masonry structures." *Journal of Structural Engineering*, 120(1), 63-80.

Lourenço, P. B. (1994). "Analysis of masonry structures with interface elements: Theory and applications." *TNO Building and Construction Research*, Faculty of Civil Engineering, Delft University of Technology, Delft, Netherlands.

Lourenço, P. B. (1996). "Computational strategies for masonry structures." PhD dissertation, Delft University of Technology, Netherlands.

Lourenco, P. B., and Rots, J. G. (1997). "Multisurface interface model for analysis of masonry structures." *Journal of Engineering Mechanics*, 123(7), 660-668.

Macorini, L., and Izzuddin, B. (2011). "A non-linear interface element for 3D mesoscale analysis of brick-masonry structures." *International Journal for Numerical Methods in Engineering*, 85(12), 1584-1608.

Metcalf, M., Reid, J., and Cohen, M. (2011). *Modern Fortran explained (numerical mathematics and scientific computation)*, Oxford University Press, New York.

Miccoli, L., Garofano, A., Fontana, P., and Müller, U. (2015). "Experimental testing and finite element modelling of earth block masonry." *Engineering Structures*, 104, 80-94.

Minga, E., Macorini, L., and Izzuddin, B. A. (2018). "A 3D mesoscale damage-plasticity approach for masonry structures under cyclic loading." *Meccanica*, 53(7), 1591-1611.

Oliveira, D. V., and Lourenço, P. B. (2004). "Implementation and validation of a constitutive model for the cyclic behaviour of interface elements." *Computers & Structures*, 82(17), 1451-1461.

Ottosen, N. S., and Ristinmaa, M. (2005). *The mechanics of constitutive modeling*, Elsevier, Amsterdam, Netherland.

Page, A. W. (1978). "Finite element model for masonry." *Journal of the Structural Division*, 104(8), 1267-1285.

Page, A. W. (1983). "The strength of brick masonry under biaxial tension-compression." *International Journal of Masonry Construction*, 3(1), 26-31.

Pelà, L. (2009). "Continuum damage model for nonlinear analysis of masonry structures." PhD dissertation, Polytechnic University of Catalonia, Barcelona, Spain.

Pérez-Foguet, A., Rodríguez-Ferran, A., and Huerta, A. (2001). "Consistent tangent matrices for substepping schemes." *Computer Methods in Applied Mechanics and Engineering*, 190(35-36), 4627-4647.

Rots, J. G., and Picavet, B. (1997). "Structural masonry: An experimental/numerical basis for practical design rules." Centre for Civil Eng Research and Codes, Netherlands.

Schellekens, J. C. J. (1992). "Computational strategies for composite structures." PhD dissertation, Delft University of Technology, Delft, Netherlands.

Shing, P. B., and Manzouri, T. "Analysis of unreinforced masonry structures using elastic/viscoplastic models." *Proc., Sísmica 2004-6º Congresso Nacional de Sismologia e Engenharia Sísmica Livro de Actas*, 137-150.

Simo, J., and Taylor, R. (1986). "A return mapping algorithm for plane stress elastoplasticity." *International Journal for Numerical Methods in Engineering*, 22(3), 649-670.

Simo, J. C., and Hughes, T. J. (2006). *Computational inelasticity*, Springer Science and Business Media, New York.

Spada, A., Giambanco, G., and Rizzo, P. (2009). "Damage and plasticity at the interfaces in composite materials and structures." *Computer Methods in Applied Mechanics and Engineering*, 198(49-52), 3884-3901.

Tang, H., Barthelat, F., and Espinosa, H. (2007). "An elasto-viscoplastic interface model for investigating the constitutive behavior of nacre." *Journal of the Mechanics and Physics of Solids*, 55(7), 1410-1438.

Tarque, N. (2011). "Numerical modelling of the seismic behaviour of adobe buildings." PhD dissertation, University of Pavia, Lombardy, Italy.

Van der Pluijm, R., Rutten, H., and Ceelen, M. (2000). "Shear behaviour of bed joints." *Proc., 12th International Brick/Block Masonry Conference*, IB2MaC, Madrid, Spain, 3, 1849-1862.

Vermeltfoort, A. T., and Raijmakers, T. (1993a). "Deformation controlled tests in masonry shear walls: Part 2." Eindhoven University of Technology, Eindhoven, Netherlands.

Vermeltfoort, A. T., and Raijmakers, T. (1993b). "Deformation controlled tests in masonry shear walls: Part 1." Eindhoven University of Technology, Eindhoven, Netherlands.

Figure Captions

Fig. 1. Typical composite failure surface for the proposed CTSIM in stress space.

Fig. 2. Hardening/softening law for compression cap failure criterion.

Fig. 3. Typical failure surface in stress space for: (a) Lourenco's model, (b) Macorini's model, and (c) Citto's model.

Fig. 4. Load paths used in the one-element test of the different constitutive models.

Fig. 5. Iso-error maps for the point on the yield surfaces at θ = 36.13°: (a) CTSIM, (b) Lourenco's model, (c) Macorini's model, and (d) Citto's model.

Fig. 6. Size of the Jacobian matrix for different regions of the constituitve models: (a) CTSIM, (b) Lourenco's model, (c) Macorini's model, and (d) Citto's model.

Fig. 7. Masonry shear walls: (a) shear walls, and (b) SMM used for simulating the shear wall.

Fig. 8. Comparison of experimental and numerical results in terms of load-displacement response of the shear wall.

Fig. 9. Comparison of experimental and numerical results: (a) and (b) experimental crack patterns for the two specimens; and deformed shaped and distribution of minimum principal stress for (c) CTSIM, (d) Lourenco's model, (e) Macorini's model, and (f) Citto's model.

Table 1. Elastic properties of masonry units, joints, and potential cracks.

Property	Value
Masonry units	
E [MPa]	16,700
υ	0.15
Joints	
k_n [N/mm^3]	82.00
k_s [N/mm^3]	36.00
Potential cracks	
k_n [N/mm^3]	10,000
k_s [N/mm^3]	10,000

Table 2. Inelastic properties for joints and potential cracks.

Property	Joints	Potential cracks
Tension-shear failure criterion		
f_t [MPa]	0.25	2.0
G_f^I [N/mm]	0.018	0.008
C_0 [MPa]	$1.45 f_t$	$1.45 f_t$
C_{Q0} [MPa]	$50 C_0$	C_0
$\tan\phi_0 / \tan\phi_r$	0.75/0.75	1.0/1.0
$\tan\psi_0 / \tan\psi_r$	0.001/0.0001	1.0/1.0
G_f^{II} [N/mm]	0.125	0.50
Compression cap failure criterion		
$\bar{\sigma}_0$ [MPa]	3.5	-
$\bar{\sigma}_p$ [MPa]	10.5	-
$\bar{\sigma}_m$ [MPa]	5.25	-
$\bar{\sigma}_r$ [MPa]	1.5	-
κ_p	0.09	-
κ_m	0.49	-

Table 3. CPU time ratio (CTR) vs percentage error (δ) for tension-shear region.

θ	N	CTSIM		Lourenco's model		Macorini's model		Citto's model	
		CTR	δ	CTR	δ	CTR	δ	CTR	δ
0	N100	0.093	<0.01	0.106	<0.01	0.106	2.62	0.087	96.45
	N50	0.050	<0.01	0.050	<0.01	0.050	5.58	0.043	>100
	N10	0.012	<0.01	0.012	<0.01	-	-	-	-
	N5	0.006	<0.01	0.006	<0.01	-	-	-	-
15	N100	0.099	<0.01	0.106	<0.01	0.113	2.26	0.134	1.67
	N50	0.042	<0.01	0.049	<0.01	0.049	4.81	0.056	>100
	N10	0.014	<0.01	0.021	<0.01	-	-	-	-
	N5	0.007	<0.01	0.007	0.02	-	-	-	-
30	N100	0.101	<0.01	0.101	<0.01	0.109	1.60	0.116	1.44
	N50	0.058	<0.01	0.051	<0.01	0.051	3.40	0.051	>100
	N10	0.014	<0.01	0.014	0.03	-	-	-	-
	N5	0.007	<0.01	0.007	0.04	-	-	-	-
45	N100	0.093	<0.01	0.099	<0.01	0.105	0.92	0.099	1.09
	N50	0.049	<0.01	0.062	<0.01	0.049	1.94	0.049	2.30
	N10	0.019	<0.01	0.019	<0.01	-	-	-	-
	N5	0.006	<0.01	0.006	67.70	-	-	-	-
60	N100	0.096	<0.01	0.110	<0.01	0.103	0.03	0.103	0.68
	N50	0.062	<0.01	0.062	<0.01	0.055	0.08	0.055	1.42
	N10	0.014	<0.01	0.021	<0.01	0.021	1.28	0.014	>100
	N5	0.007	<0.01	0.007	>100	-	-	-	-
75	N100	0.097	<0.01	0.090	<0.01	0.111	0.10	0.097	0.29
	N50	0.056	<0.01	0.049	<0.01	0.056	0.21	0.049	0.61
	N10	0.014	<0.01	0.014	<0.01	0.014	1.67	0.014	4.04
	N5	0.007	0.03	0.007	37.87	0.007	1.83	0.007	10.16
90	N100	0.097	0.42	0.103	0.02	0.109	0.35	0.085	0.22
	N50	0.048	0.87	0.048	0.04	0.055	0.72	0.042	0.46
	N10	0.012	3.42	0.012	0.33	0.018	3.50	0.018	2.60

	N5	0.006	5.90	0.006	1.46	0.012	8.37	0.006	4.58

Table 4. CPU time ratio (CTR) vs percentage error (δ) for compression-shear region.

θ	N	CTSIM		Lourenco's model		Macorini's model		Citto's model	
		CTR	δ	CTR	δ	CTR	δ	CTR	δ
105	N100	0.105	0.02	0.105	0.01	0.112	0.03	0.112	0.12
	N50	0.049	0.05	0.056	0.02	0.042	0.31	0.042	0.29
	N10	0.014	0.39	0.014	0.33	0.014	3.53	0.014	1.09
	N5	0.007	0.76	0.007	0.45	0.007	10.39	0.007	1.72
120	N100	0.101	0.06	0.109	0.06	0.109	0.05	0.109	6.19
	N50	0.051	0.12	0.065	0.13	0.051	0.11	0.051	7.19
	N10	0.014	1.17	0.014	1.31	0.014	3.16	0.014	10.60
	N5	0.007	49.53	0.007	54.68	0.007	73.19	0.007	>100
135	N100	0.102	0.07	0.102	0.08	0.102	0.11	0.109	0.57
	N50	0.054	0.14	0.048	0.16	0.048	0.24	0.051	1.23
	N10	0.014	1.32	0.014	1.54	0.014	0.60	0.014	57.20
	N5	0.007	35.45	0.007	35.56	0.007	52.46	0.007	>100
150	N100	0.094	0.05	0.101	0.07	0.081	0.12	0.107	0.65
	N50	0.054	0.11	0.054	0.14	0.047	0.24	0.040	1.34
	N10	0.013	1.03	0.013	1.26	0.013	2.24	0.013	98.96
	N5	0.007	49.10	0.007	48.81	-	-	-	-
165	N100	0.104	0.02	0.090	0.03	0.097	0.02	0.111	0.14
	N50	0.056	0.05	0.042	0.06	0.049	0.05	0.049	0.20
	N10	0.014	0.81	0.014	0.57	0.014	0.32	0.021	11.19
	N5	0.007	55.63	0.007	54.73	0.007	61.02	-	-
180	N100	0.097	<0.01	0.097	<0.01	0.103	0.01	0.097	1.18
	N50	0.055	<0.01	0.055	<0.01	0.055	0.02	0.055	2.10
	N10	0.014	<0.01	0.014	<0.01	0.014	0.22	0.014	13.43
	N5	0.007	59.35	0.007	57.99	-	-	-	-

Table 5. Load increments and CPU time ratio for different constitutive models in the analysis of the benchmark masonry shear wall.

Item	CTSIM	Lourenco's model	Macorini's model	Citto's model
Increments	26,620	29,679	35,564	40,119
Cutback	6,796	7,861	9,538	11,137
Total iterations	106,567	114,378	136,680	170,495
CPU time ratio (CTR)	1.00	1.37	1.22	1.48

Table 6. Number of iterations under different conditions for different models.

	CTSIM		Lourenco's model		Macorini's model		Citto's model	
Violation of failure criterion	Iteration (Millions)	%	Iteration (Millions)	%	Iteration (Millions)	%	Iteration (Millions)	%
Rankine	-	-	0.52	1.89	-	-	29.81	100
Mohr-Coulomb	-	-	18.47	66.74	-	-		
Tension-shear	17.96	82.60	-	-	24.42	98.58		
Compression cap	3. 01	16.58	2.93	10.58	0.32	1.31		
T-S corner*	-	-	5.59	20.19	-	-		
S-C corner**	0.18	0.82	0.17	0.60	0.03	0.11		
Total	**21.15**		**27.68**		**24.77**		**29.81**	

* Multi-surface singularity between Rankine and Mohr-Coulomb failure criterion

** Multi-surface singularity between Mohr-Coulomb or tension-shear and compression cap failure criterion

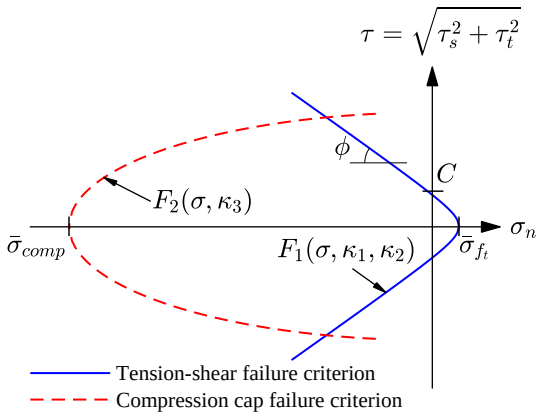
$\tau = \sqrt{\tau_s^2 + \tau_t^2}$
ϕ
C
$F_2(\sigma, \kappa_3)$
σ_n
$\bar{\sigma}_{comp}$
$F_1(\sigma, \kappa_1, \kappa_2)$
$\bar{\sigma}_{f_t}$
Tension-shear failure criterion
Compression cap failure criterion

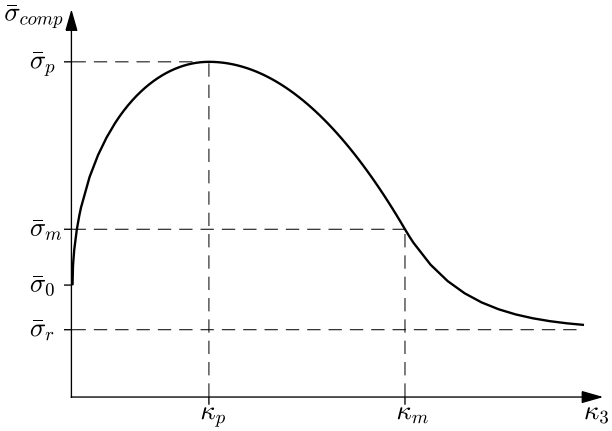
$\bar{\sigma}_{comp}$
$\bar{\sigma}_p$
$\bar{\sigma}_m$
$\bar{\sigma}_0$
$\bar{\sigma}_r$
κ_p
κ_m
κ_3

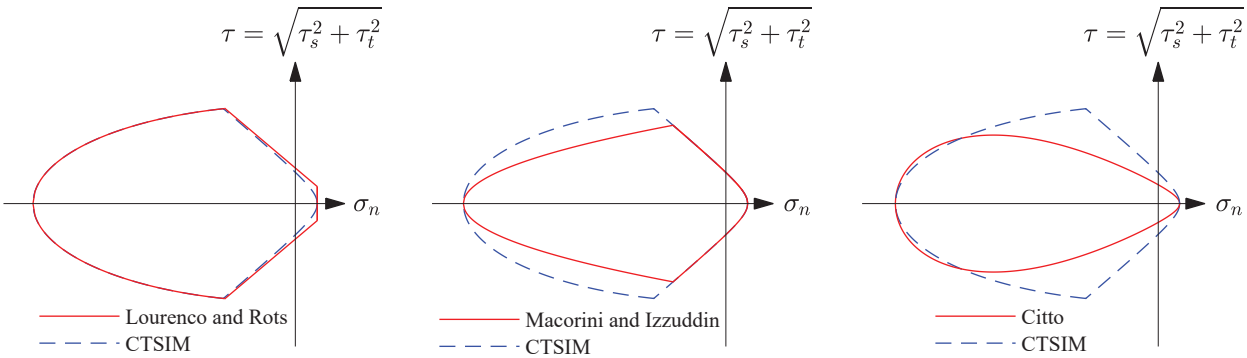
$\tau = \sqrt{\tau_s^2 + \tau_t^2}$
σ_n
Lourenco and Rots
CTSIM
(a)
$\tau = \sqrt{\tau_s^2 + \tau_t^2}$
σ_n
Macorini and Izzuddin
CTSIM
(b)
$\tau = \sqrt{\tau_s^2 + \tau_t^2}$
σ_n
Citto
CTSIM
(c)

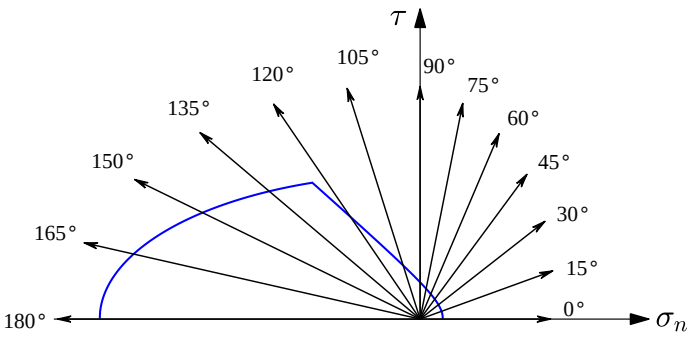
τ
105°
90°
120°
75°
135°
60°
150°
45°
30°
165°
15°
180°
0°
σ_n

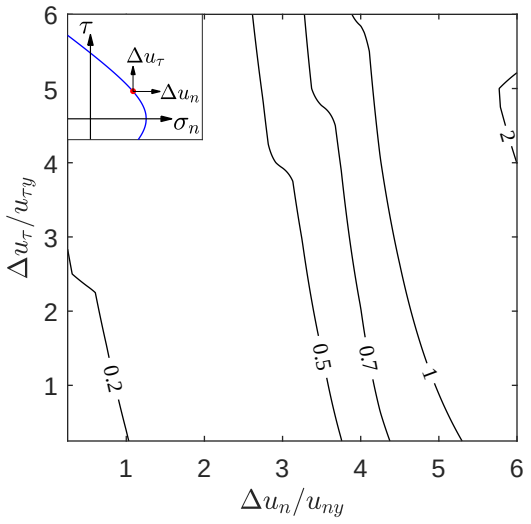
τ
Δu_τ
Δu_n
σ_n
0.2
0.5
0.7
1
2
$\Delta u_\tau / u_{\tau y}$
$\Delta u_n / u_{ny}$

(a)

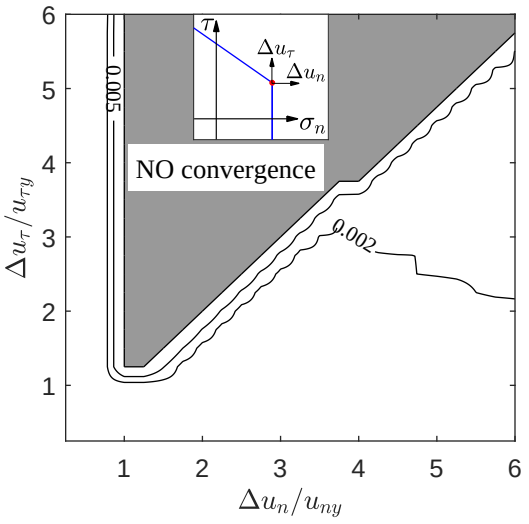
τ
Δu_τ
Δu_n
σ_n
0.005
0.002
NO convergence
$\Delta u_\tau / u_{\tau y}$
$\Delta u_n / u_{ny}$

(b)

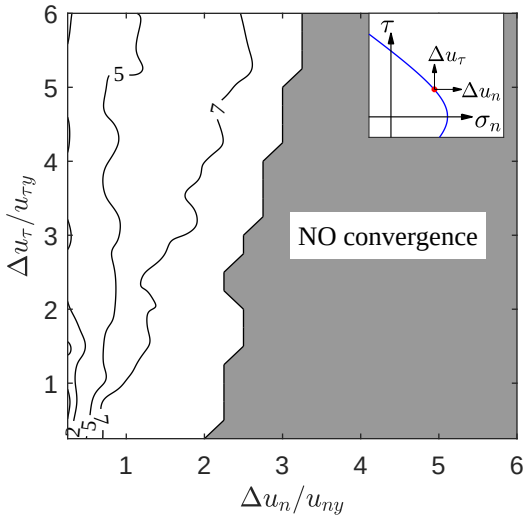
τ
Δu_τ
Δu_n
σ_n
5
7
NO convergence
$\Delta u_\tau / u_{\tau y}$
$\Delta u_n / u_{ny}$

(c)

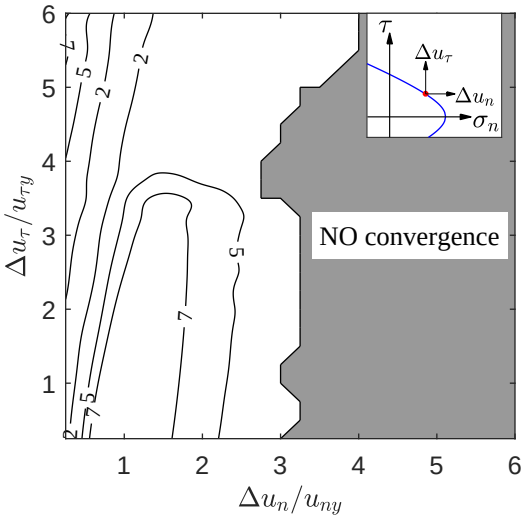
τ
Δu_τ
Δu_n
σ_n
2
5
7
NO convergence
$\Delta u_\tau / u_{\tau y}$
$\Delta u_n / u_{ny}$

(d)

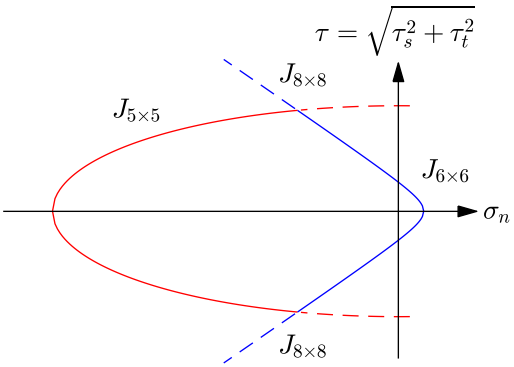
$\tau = \sqrt{\tau_s^2 + \tau_t^2}$
$J_{8\times8}$
$J_{5\times5}$
$J_{6\times6}$
σ_n
$J_{8\times8}$

(a)

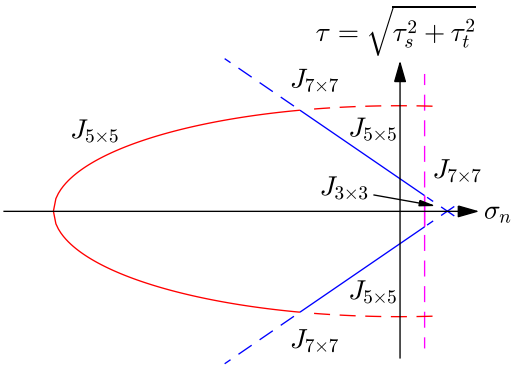
$\tau = \sqrt{\tau_s^2 + \tau_t^2}$
$J_{7\times7}$
$J_{5\times5}$
$J_{5\times5}$
$J_{7\times7}$
$J_{3\times3}$
σ_n
$J_{5\times5}$
$J_{7\times7}$

(b)

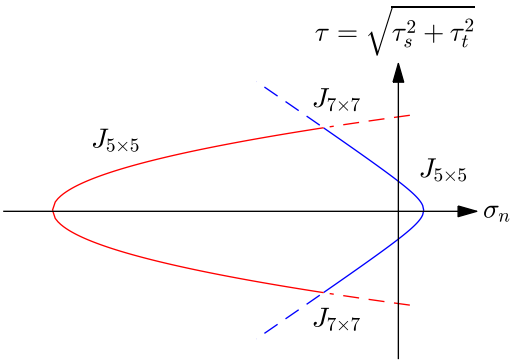
$\tau = \sqrt{\tau_s^2 + \tau_t^2}$
$J_{7\times7}$
$J_{5\times5}$
$J_{5\times5}$
σ_n
$J_{7\times7}$

(c)

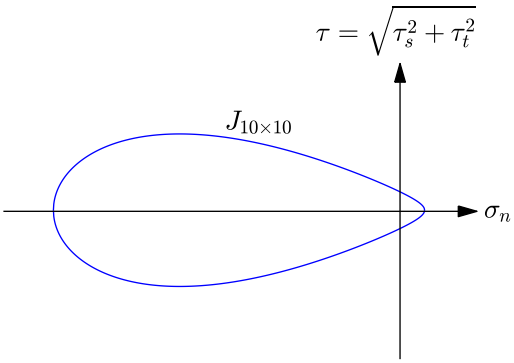
$\tau = \sqrt{\tau_s^2 + \tau_t^2}$
$J_{10\times10}$
σ_n

(d)

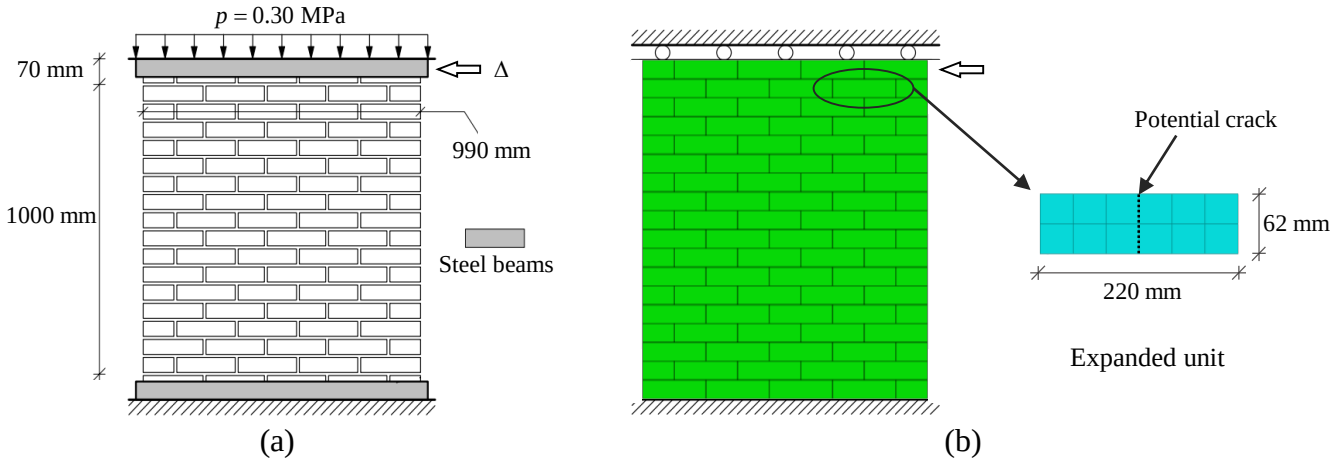
p = 0.30 MPa
70 mm
Δ
990 mm
1000 mm
Steel beams
(a)
Potential crack
62 mm
220 mm
Expanded unit
(b)

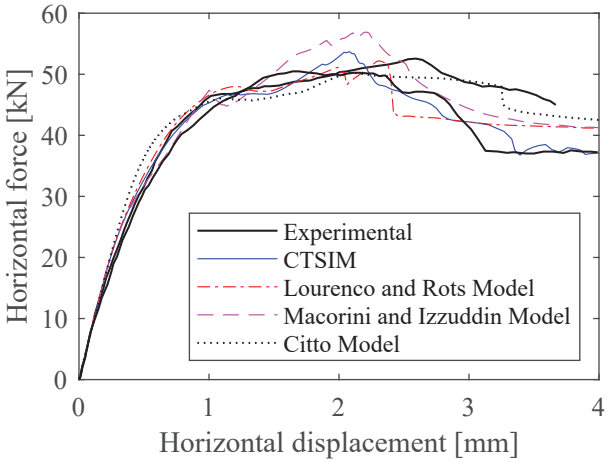
Horizontal force [kN]
Horizontal displacement [mm]
0
10
20
30
40
50
60
0
1
2
3
4
Experimental
CTSIM
Lourenco and Rots Model
Macorini and Izzuddin Model
Citto Model

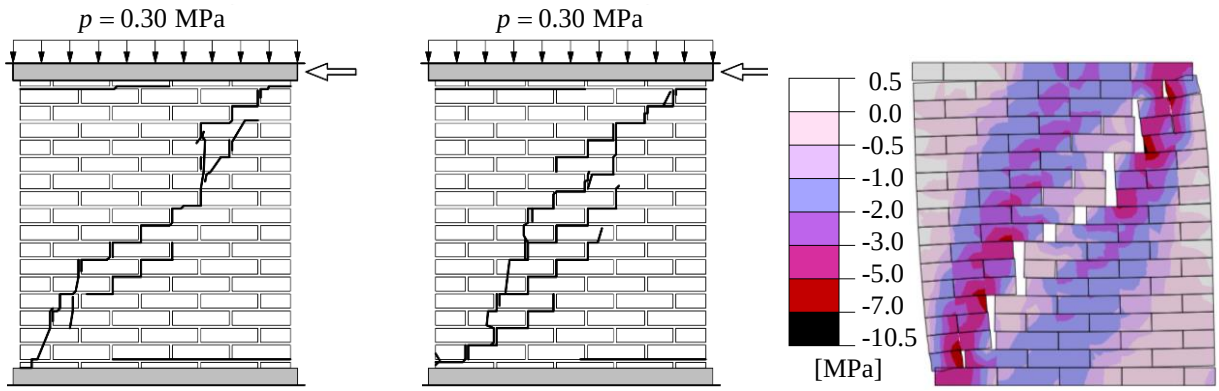

(a) (b) (c)

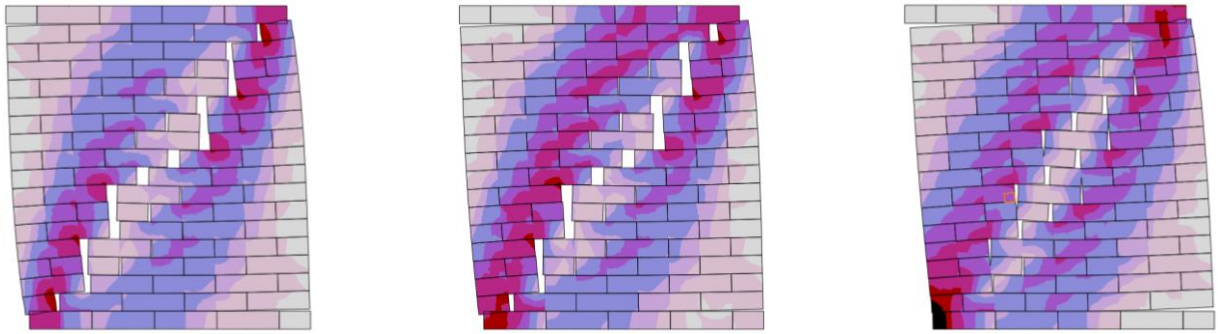

(d) (e) (f)